Benchmark Study on Rotor Performance, Wake Dynamics, and Atmospheric Boundary Layers using NREL SOWFA-6 and AMR-WIND

Dammann, Tim; Dangi, Nirav; Wingerden, Jan-Willem Van; Yu, Wei

DOI
10.1088/1742-6596/3016/1/012034

Publication date
2025

Document Version
Final published version

Published in
Journal of Physics: Conference Series

Benchmark Study on Rotor Performance, Wake Dynamics, and Atmospheric Boundary Layers using NREL SOWFA-6 and AMR-WIND

Journal of Physics: Conference Series **3016** (2025) 012034 doi:10.1088/1742-6596/3016/1/012034

Benchmark Study on Rotor Performance, Wake Dynamics, and Atmospheric Boundary Layers using NREL SOWFA-6 and AMR-WIND

Tim Dammann[1,*], Nirav Dangi[2,*], Jan-Willem van Wingerden[1], and Wei Yu[2]

[1]Mechanical Engineering, Delft University of Technology, 2628 CD Delft, The Netherlands
[2]Aerospace Engineering, Delft University of Technology, 2629 HS Delft, The Netherlands
[*]These authors contributed equally to this work

E-mail: T.Dammann@tudelft.nl

Abstract. Benchmarking numerical models is essential for validating their accuracy and ensuring consistency across simulation platforms. This study presents a comparative benchmark analysis of two widely used Large Eddy Simulation (LES) codes, AMR-WIND and NREL SOWFA-6, focusing on wind turbine rotor performance, wake dynamics, and atmospheric boundary layer (ABL) representation. The evaluation includes an actuator line model (ALM)-based uniform inflow wind turbine simulation and ABL precursors under neutral and unstable conditions. The uniform inflow wake analysis examined differences in wind turbine induction and wake development between the two codes. Additionally, neutral and unstable atmospheric boundary layer precursors were generated for an offshore environment and compared. Results indicate a difference in wake breakdown location between the codes (one contributing factor was the difference in numerical schemes used for the advection terms.) The number of actuator points required for smooth velocity distribution across the rotor was higher for SOWFA-6 than AMR-WIND. In ABL precursors, time-averaged flow fields showed strong agreement, though minor discrepancies in turbulence were observed, particularly in unstable conditions, affecting coherence analysis. The energy distribution across wavenumbers showed a good match between the codes, with slight discrepancies observed in the large and small wavenumber regions. The cutoff wavenumber was found to be similar for both codes. Lateral and vertical coherence at small and large separations were in close agreement for the neutral ABL. However, in the unstable ABL, notable differences in coherence were observed between the codes for separations greater than 40 m.

1 Introduction

Wind energy has become a crucial component of the global renewable energy transition, with large-scale offshore and onshore wind farms contributing significantly to electricity generation. Understanding wind turbine wake dynamics and their interactions with the atmospheric boundary layer (ABL) is essential for optimizing energy capture, reducing turbine loads, and improving wind farm design. Large Eddy Simulation (LES) techniques have emerged as powerful tools to study these phenomena, providing high-fidelity insights into wake behavior and turbulence characteristics [1, 2].

Recent advancements in LES-based wind energy simulations have been driven by the development of computational frameworks such as the Simulator fOr Wind Farm Applications (SOWFA) [3] and Adaptive Mesh Refinement for Wind (AMR-WIND) [4]. These codes enable high-resolution modeling of wind turbine aerodynamics, wake formation, and ABL interactions under varying atmospheric conditions [5]. While both SOWFA-6 and AMR-WIND leverage actuator line modeling (ALM) to represent turbine-induced flow effects, differences in numerical schemes, spatial discretization, and subgrid-scale turbulence modeling can influence simulation accuracy and wake predictions [6].

The main contribution of this paper is twofold: (1) it provides a comprehensive benchmark comparison of SOWFA-6 and AMR-WIND, evaluating their capabilities in simulating rotor performance, wake dynamics, and atmospheric boundary layer (ABL) representation; (2) it assesses key numerical characteristics of each solver, including numerical dissipation, turbulence coherence, velocity profiles, and Reynolds stresses, by analyzing uniform inflow wake characteristics and precursor ABL simulations under neutral and unstable conditions. The IEA 22 MW reference wind turbine [7] is tested as a standardized case to facilitate direct comparisons of force distributions, velocity deficits, and spectral energy distributions.

The findings contribute to the broader effort of improving LES methodologies for wind energy applications. By identifying strengths and limitations in current simulation techniques, this work informs the development of more accurate and computationally efficient modeling approaches. Future studies incorporating additional solver comparisons and experimental validations will enhance confidence in LES-based wind farm modeling.

The remainder of this paper is structured as follows: Section 2 details the numerical methods and simulation setup, including the implementation of actuator line models and atmospheric boundary layer precursors. Section 3 presents the results of the uniform inflow wake analysis, focusing on rotor forces, velocity distributions, and wake dynamics. Section 4 discusses the comparison of precursor ABL simulations under different stability conditions. Finally, Section 5 summarizes the key findings, outlines the study's implications, and suggests directions for future research.

2 Numerical methods

NREL SOWFA-6 [5, 3] and AMR-WIND [4] were utilized to conduct ALM-based wind turbine wake analysis and generate atmospheric boundary layer precursors in varying atmospheric stability conditions. SOWFA is an LES solver developed by the National Renewable Energy Laboratory (NREL) that is specifically designed for wind farm modeling. It is implemented within the OpenFOAM framework [8] and employs the finite-volume approach. The LES code AMR-Wind [4] is an adaptive-mesh incompressible Navier-Stokes solver designed for wind turbine and wind farm simulations by the NREL. It is built on top of the AMReX library [9], solving the governing equations on a block-structured cartesian grid which can be locally refined. The spatial discretization in AMR-WIND combines the finite volume and finite-difference methods. Important spatial and temporal discretization aspects in AMR-WIND are discussed in [6]. In both solvers, the second-order accurate Crank-Nicolson time scheme was used. For spatial discretization, in line with [6], the WENO-Z scheme [10] was used in AMR-WIND for the advection terms, exhibiting fifth-order accuracy. The advection terms were discretized using a fourth-order scheme (closest equivalent available to the WENO-Z scheme) in SOWFA-6. Other terms were discretized with second-order accuracy. Both codes allow for actuator line-based structural coupling with NREL OpenFAST [11], which is utilized in this study.

The spatially filtered, incompressible Navier–Stokes equations to give the resolved-scale (large-eddy scale) fluid flow dynamics were solved, incorporating the filtered continuity equation as shown in Equation 1. The nomenclature from [1] is utilized.

$$\frac{\partial \bar{u}_j}{\partial x_j} = 0 \tag{1}$$

where the overbar denotes spatial filtering and $\bar{u}_j = u_j - u_j^{'}$ is the resolved-scale velocity vector, which is the instantaneous velocity vector, u_j, minus the subfilter-scale (SFS) velocity vector, $u_j^{'}$. The filtered

momentum equation is shown in Equation 2

$$\frac{\partial \bar{u}_i}{\partial t} + \frac{\partial}{\partial x_j}\left(\bar{u}_j \bar{u}_i\right) = -\underbrace{2\epsilon_{i3k}\Omega_3 \bar{u}_k}_{\text{I}} - \underbrace{\frac{\partial \tilde{p}}{\partial x_i}}_{\text{II}} \underbrace{- \frac{1}{\rho_0}\frac{\partial}{\partial x_i} p_0(x,y)}_{\text{III}} \underbrace{- \frac{\partial \tau_{ij}^D}{\partial x_j}}_{\text{IV}} \underbrace{+ g\left(\frac{\bar{\theta} - \theta_0}{\theta_0}\right)\delta_{i3}}_{\text{V}} + \underbrace{\frac{1}{\rho_0} F_i^T}_{\text{VI}} \tag{2}$$

Term I is the Coriolis force due to planetary rotation, and ϵ_{ijk} is the alternating tensor. The rotation rate vector is given by Ω_j, as, $\Omega = \omega[0, \cos(\phi), \sin(\phi)]$, where ω is the planetary rotation rate and ϕ is the latitude. This study used a latitude of 52.8°, representing the Dutch North Sea [12], for the atmospheric boundary layer precursors. Term II is the gradient of the modified pressure variable. Term III represents the background driving pressure gradient, and Term IV accounts for the divergence of the deviatoric fluid stress tensor, which includes viscous and SFS components. Term V models buoyancy effects via the Boussinesq-approximation, while Term VI accounts for other density-normalized forces, such as those in an actuator line turbine model. The transport equation for resolved potential temperature is given in Equation 3, where q_j represents temperature flux due to viscous and SFS effects. The following subsections outline the set-up for uniform inflow wake and atmospheric boundary layer simulations.

$$\frac{\partial \bar{\theta}}{\partial t} + \frac{\partial}{\partial x_j}\left(u_j \bar{\theta}\right) = -\frac{\partial q_j}{\partial x_j} \tag{3}$$

2.1 Uniform Inflow

The wind turbine utilized was the IEA-22MW reference model [7], with a rotor diameter of D=283.2 m. The computational domain follows the layout described in [2]. The stream-wise dimension is $L_x = 24\,\text{D}$, whereas the lateral and vertical dimensions are $L_{y,z} = 6\,\text{D}$. The isotropic grid has a mesh size of 10 m at level 0 with a single refinement sharing its centroid with the turbine rotor. It starts 1.5 D upstream of the rotor and extends 8.5 D in a streamwise direction. The lateral dimension has an overall extent of 3 D, leading to approximately 56 cells per rotor diameter. A mass inflow condition is applied to the inlet boundary, and a pressure outflow condition is applied to the outlet boundary. All lateral boundaries have slip-wall conditions. The Coriolis forcing was neglected by specifying the Earth's rotation period to a large number, here, 10^{10} hr. The turbine rotor is modeled without a tower and nacelle. It is located in the lateral center of the domain, with a distance of 3 D from the inlet boundary. The rotor is modeled as a rigid body with no pre-cone and no shaft tilt. The Gaussian smearing of the actuator point forces is chosen as $\epsilon = 10$, leading to an epsilon by grid (EBG) ratio of $\epsilon/\Delta_x = 2$. Based on prior observations of the authors, the number of actuator points was set to 59 (equal to number of defined airfoil sections) for AMR-WIND, and 75 in the case of SOWFA-6. Any other amount resulted in jagged velocity deficit profiles at the rotor. A uniform inflow was set, coming from 270° (westward, in meteorological convention) with a constant wind speed of $u_\infty = 8\,\text{m/s}$. The time step of the simulation was set to $\Delta t = 0.06\,\text{s}$ to comply with the ALM restriction of $\frac{u_{tip}\Delta t}{\Delta x} < C_{max}$ with $C_{max} = 1$, given the design tip speed for u_∞ as 74.14 m/s and considering a rotational speed of $\Omega = 5\,\text{rpm}$ [13]. Hence, the resulting tip speed ratio (TSR) amounts to $\lambda = 9.25$. In all uniform inflow simulations, the Smagorinsky turbulence model was used to capture subgrid-scale effects. In AMR-Wind , a constant Smagorinsky coefficient of $C_s = 0.135$ was employed. Similarly, in SOWFA-6, the inputs C_ϵ and C_k were set to 1.077 and 0.071 respectively evaluating the expression $C_s = \left(C_k \sqrt{\frac{C_k}{C_\epsilon}}\right)^{\frac{1}{2}}$ [14]. Velocity data was sampled linearly at the actuator points. The simulation was run for a total duration of 1680 s, comprising an initial spin-up period of one flow-through time of $\frac{L_x}{u_\infty} = 840\,\text{s}$ to eliminate transient effects, followed by a sampling period of another flow-through period.

2.2 ABL Simulations

The details of the precursor setup can be found in [15], and simulation inputs are concisely provided here. All ABL simulations were conducted, using the eddy-viscosity SFS model from [16, 17]. A domain width, length, and altitude of 3 km, 4.5 km, and 1 km, respectively was used. An isotropic grid of 10 m size was employed in both codes. A hub height wind speed control was set to 11.5 m/s at 170 m altitude from the west boundary face (implying a 270° wind direction). The neutral ABL precursor was run with

0 Km/s surface flux, while the unstable ABL precursor was run with a surface flux of 0.02 Km/s. Velocity perturbations of 0.25 m/s near the surface were used in both codes to aid in turbulence generation and yield a similar initial transient and further profile development. The neutral and unstable ABL precursors used a capping inversion of 500 m. A surface roughness of 0.0001 m was used in both the precursors, and the simulations were run for a period of 21000 s with a time step of 0.5 s, of which the last 1000 s were used for result analysis.

3 Results: Uniform Inflow Wake Analysis

The two codes' spanwise force distributions obtained in uniform inflow are presented in subsection 3.1, followed by the discussion of global forces in subsection 3.2. The velocity deficit and Reynolds stresses are presented in subsection 3.3. The CPU time for SOWFA-6 in the case of the uniform inflow simulations amounted to 555 days, whereas AMR-Wind showed a faster computational time of 358 days, which is an increase of 35 %.

3.1 Spanwise Force Distributions

Figure 1 presents the spanwise distribution of aerodynamic forces as the two LES solvers predicted. The forces were computed as time-averaged values over 60 complete rotor revolutions, with data extracted at nine uniformly distributed spanwise locations along the rotor blade. For reference, blade element momentum (BEM) theory calculations, excluding tip-loss corrections, were utilized as a baseline comparison. The ALM simulations were also conducted without tip-loss correction.

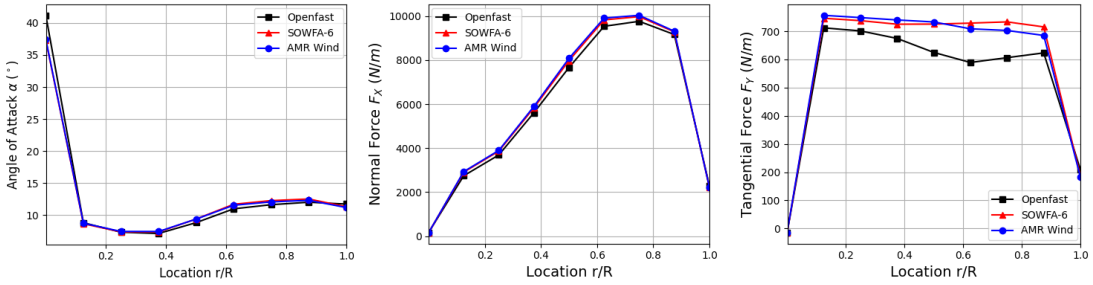

(a) (b) (c)

Figure 1: Spanwise distributions of angle of attack, normal force (to plane) F_X, and tangential force (to plane) F_Y.

The spanwise variation of the angle of attack (AoA) (Figure 1a) reveals strong overall agreement between the two solvers, demonstrating consistency in capturing the aerodynamic loading trends. Between $0.5r/R$ and $0.9r/R$, both solvers show AoA values, approximately 0.5° higher than the BEM solution, which partially explains the higher F_X and F_Y values in Figure 1b and Figure 1c respectively. The chosen ϵ-value of 10 m likely results in slight force overestimation. A prior study [18] found that the force predicted by LES solvers is affected by the chosen grid size and ϵ-value (see Figure 6 of their study) and usually leads to overestimations for higher ϵ-values. While this value provides reasonable accuracy near the nacelle region, where the blade geometry is characterized by a larger chord length, the deviation increases progressively toward the blade tip. The blade chord decreases from a maximum of approximately 7 m near the root to less than 1 m at the tip. Consequently, an ϵ-value of 10 m is no longer suitable for accurately resolving the smaller tip region. To achieve more accurate force predictions, one could consider employing a smaller ϵ-value in conjunction with a finer local grid resolution or a filtered lifting line method, where ϵ is scaled with the local chord length [19]. However, both approaches would result in a significant increase in computational cost. Furthermore, as the primary objective of this study is to compare the performance of the two solvers, we accept the observed over-estimations as part of the inherent limitations of the chosen modeling approach. Comparative analysis further indicates that SOWFA-6 tends to overestimate tangential forces more significantly than AMR-Wind for $r/R \geq 0.6$. This is reflected in the global forces in Figure 2. At the same time, AMR-Wind exhibits a stronger overestimation in the lower spanwise region of the blade. These discrepancies highlight subtle differences in the numerical treatments and turbulence modeling strategies the solvers employ.

3.2 Global forces

Figure 2 presents the time series of global forces acting on the turbine rotor. Both LES solvers demonstrate convergence at approximately 400 s. The time series of the thrust force, shown in Figure 2a, indicates that while both solvers achieve convergence, SOWFA-6 demonstrates more pronounced fluctuations around the mean compared to AMR-Wind. The time history for SOWFA-6 displays irregular oscillations around the mean value, whereas AMR-Wind exhibits significantly smaller variations with a more stable behavior. An examination of the force distribution curves reveals distinct characteristics for the two solvers. Force distribution curves show that SOWFA-6's thrust force follows a broad normal distribution, whereas AMR-Wind produces a more discrete, tightly clustered distribution. A similar trend appears in power output (Figure 2b), where SOWFA-6 predicts a wider range of extreme values and slightly higher overall power due to increased tangential forces along the second half of the blade (subsection 3.1). The flapwise bending moment (Figure 2c) follows the same pattern, with SOWFA-6 showing higher-frequency fluctuations, although a low-frequency signal smooths the overall distribution. SOWFA-6's probability distribution follows a double-Gaussian profile, indicating multiple force states, while AMR-Wind's distribution clusters near extreme values, reflecting structured but constrained variability.

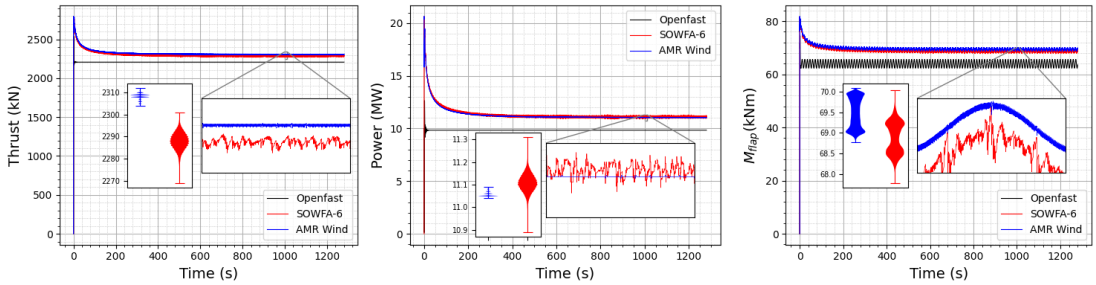

(a) (b) (c)

Figure 2: Time series of thrust, power, and flapwise bending moment for the IEA-22MW turbine, computed using the OpenFAST, SOWFA-6 and AMR-Wind.

3.3 Velocity Distributions

Firstly, as mentioned previously, the number of actuator points was set to 75 in SOWFA-6 while 59 in AMR-WIND. Figure 3 illustrates the motivation for this difference, showcasing the jagged velocity profile at the rotor with lower number of actuator points. Next, as shown in Figure 4, the flow fields in the near wake exhibit similar characteristics in both solvers due to the use of comparable actuator line methodologies and initial flow conditions. However, the results indicate a later wake breakdown in AMR-Wind compared to SOWFA-6. The wake in SOWFA-6 dissipates slightly earlier, around 7 D, while in AMR-Wind, it occurs closer to 8 D. One reasoning for these differences could be due to the numerical scheme. The fourth-order numerical scheme used for the advection terms in SOWFA-6 exhibits comparatively more numerical diffusion than the fifth-order like WENO-Z scheme used for the advection terms in AMR-WIND. This was further validated by utlizing a lower-order scheme in SOWFA-6 and assessing the wake breakdown (not shown here for brevity).

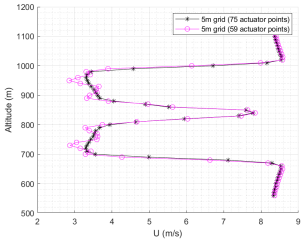

Figure 3: An illustration of the sensitivity of the SOWFA-6 results to the number of actuator points.

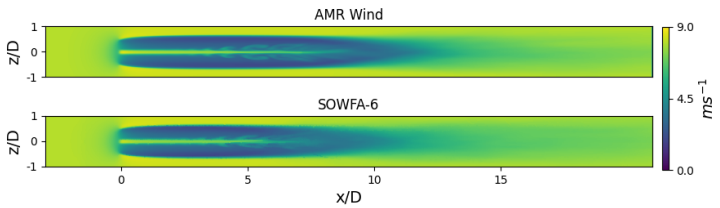

Figure 4: Mean stream-wise velocity distribution for uniform inflow conditions.

The WENO-Z scheme excels at providing least oscillations and advecting discontinuities, thus, suppressing the transition to turbulence. However, it should be noted that it is still arguable which scheme and code is more accurate in representing the true wake breakdown location given that the present study does not present comparison with measurements. One may use the higher-order scheme considering that the error will theoretically be lower, scaling with the mesh size to the power of the order of accuracy [20]. Furthermore, it is hypothesized that in non- uniform and unsteady inflow conditions, the instabilities caused by the wake and turbulence will reduce the differences caused by choice of numerical schemes. For instance, the ABL precursor comparison provided below does not show such large differences in, for example, the standard deviation and the energy spectrum of the wind speed. Another reasoning for the differences in wake breakdown may be attributed to the higher variance in the loads of the wind turbine in SOWFA-6 (Figure 2). However, at this stage, this hypothesis has not been verified and is a topic of further investigation.

The velocity profiles (upper plot) and Reynolds stress profiles (lower plot) in Figure 5 provide further insight into wake dynamics. The velocity deficit in the wake is well captured by both solvers, with the characteristic double-Gaussian velocity profile transitioning to a more uniform shape downstream. Reynolds stresses in SOWFA-6 start to form between 4 D and 5 D at the outer wake boundaries, likely induced by tip vortices. Upon that, they transition to the center of the wake at around 8 D, arranging themselves in a consistent pattern with a maximum in the wake center. In contrast, AMR-Wind shows a delayed onset of Reynolds stress development, with noticeable stress formation starting at the outer boundary of the wake after 6 D forming a double Gaussian distribution with peaks at the outer wake boundary which persists until 12 D.

This delayed stress formation in AMR-Wind aligns with the stabilization effect of its lower numerical dissipation, which suppresses turbulence in the near wake region.

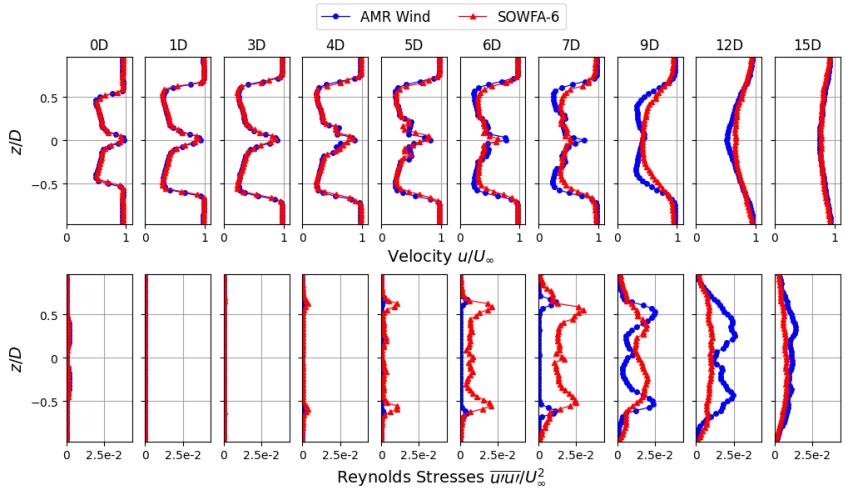

Figure 5: Normalized streamwise velocity and Reynolds stresses profiles for uniform inflow conditions at several downstream distances.

The earlier and more evenly distributed Reynolds stresses in SOWFA-6 result in a faster wake breakdown and transition of the mean velocity profile from a double-Gaussian structure to a single-Gaussian shape, occurring between 5 D and 7 D. Meanwhile, AMR-Wind maintains a double-Gaussian velocity profile until approximately 7 D. However, beyond 7 D, the magnitude of Reynolds stresses in AMR-Wind surpasses those in SOWFA-6. This sharp increase in Reynolds stresses corresponds to the onset of more abrupt wake breakdown in AMR-Wind, eventually leading to similar velocity distributions for both solvers beyond 12 D.

The plot also reveals subtle differences in the spreading and symmetry of the velocity and stress profiles. While SOWFA-6 exhibits slightly more pronounced asymmetry in both profiles, AMR-Wind demonstrates a more consistent, symmetric distribution. This difference may reflect variations in the treatment of tip vortices and hub dynamics between the two solvers, as well as differences in subgrid-scale modeling and numerical dissipation.

4 Results: Precursor Atmospheric Boundary Layer Comparisons

The NABL simulation required 158 CPU days for both codes, while the USABL simulation took 178 CPU days in the case of SOWFA-6 and 182 CPU days in the case of AMR-Wind. The time domain results of the precursors generated by the two codes in neutral and unstable atmospheric conditions are discussed in subsection 4.1, and the spectral analysis is discussed in subsection 4.2.

4.1 Flow-field comparison

Firstly, visual inspection of the contours of the instantaneous velocity components revealed the similar structures generated by the two codes (not shown here for brevity). A more quantitative insight into the flow- fields generated by the codes is provided by time and planar averaged profiles in Figure 6. The potential temperature profiles resulting from the codes (Figure 6a) match almost perfectly and obey the initial settings imposed. The time-averaged velocity components are highly consistent between the codes (Figure 6b). A similar shear in the v-component has been found between the codes owing to the Coriolis forcing, among other factors. The wind-veer also reflects this (Figure 6d). Regarding the turbulence intensity, it can be seen that up until the inversion layer, SOWFA-6 results in lower turbulence compared to the results of AMR-WIND. However, the difference is small (up to 1% at altitudes swept by the rotor). A wind veer of up to 15° has been observed in the results of both codes.

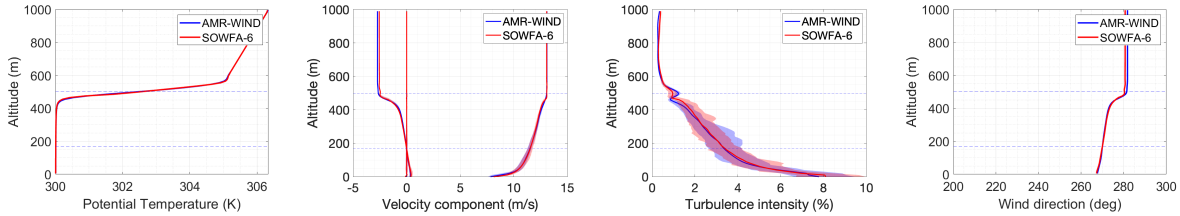

(a) Potential temperature (b) Velocity components (c) Turbulence intensity (d) Wind direction

Figure 6: Time and planar averaged flow-field parameters for the neutral atmospheric boundary layer precursors generated by AMR-WIND and SOWFA-6.

The instantaneous contours of the velocity components at the west boundary in the resulting unstable atmosphere flow- fields of the two codes were found to be similar (not shown here for brevity) as also seen for the neutral atmosphere. The time-averaged profiles shown in Figure 7 show the close agreement between the codes in various result metrics. Given the surface flux setting utilized, a moderately unstable atmosphere has been achieved in the code, as evident from the slightly negative potential temperature gradient in Figure 7a. A very low wind shear typical of unstable atmospheric conditions is evident from the u-component profile in Figure 7b. Once again, minor discrepancies are observed in the turbulent intensity (Figure 7c), a lower value for SOWFA-6 results, while higher for AMR-WIND at altitudes swept by the rotor. The overshoot in turbulence at first grid height is higher in SOWFA-6, similar to the neutral atmosphere precursor (Figure 6c). As expected, a lower wind veer than in the neutral atmosphere is observed, at roughly 5° until the capping inversion.

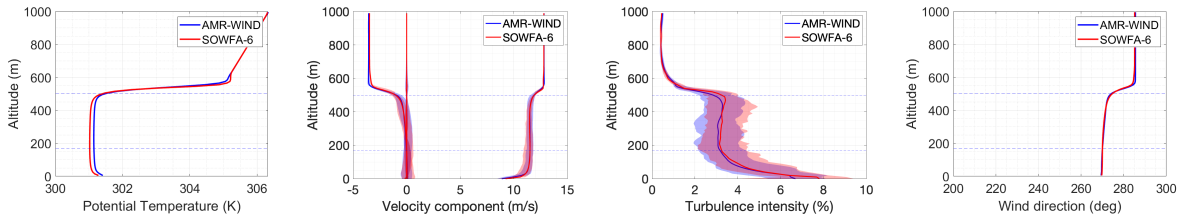

(a) Potential temperature (b) Velocity components (c) Turbulence intensity (d) Wind direction

Figure 7: Time and planar averaged flow-field parameters for the unstable atmospheric boundary layer precursors generated by AMR-WIND and SOWFA-6.

4.2 Spectral Analysis

The planar averaged energy spectrum of the u-component resulting from the two codes, at various altitudes at the west boundary of the neutral atmospheric stability precursor is shown in Figure 8. First, it can be observed that the energy distribution across different wavenumbers in the two codes is fairly similar, apart from the low wavenumber range. The low wavenumber, low-frequency structures contain lower energy in SOWFA-6 than in AMR-WIND. Both the codes yield a similar cut-off wavenumber, the wavenumber beyond which Kolmogorov's 5/3 law is not followed. This result showcases the similar limitations of the codes in resolving the high-frequency small-scale structures at the given grid size.

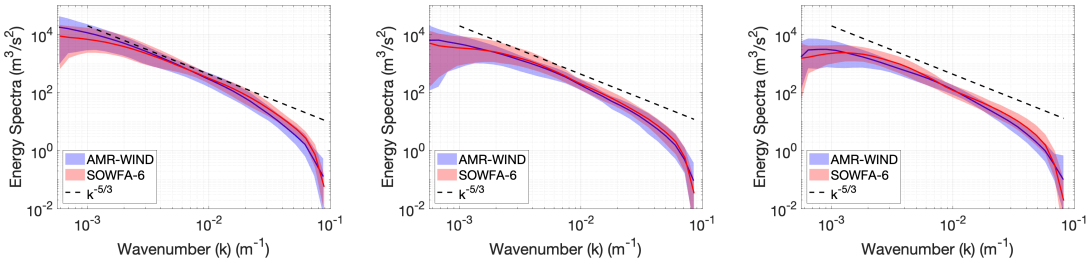

(a) Altitude of 60 m (b) Altitude of 100 m (c) Altitude of 180 m

Figure 8: Energy spectrum for the neutral atmospheric boundary layer precursors generated by AMR-WIND and SOWFA-6, at different altitudes.

Next, in-depth insight into the spectral characteristics of the flow field is aided by coherence analysis shown in Figure 9. The reader is referred to section 2.3 in [15] or [21] for details into the formulations. In this study, the coherence was calculated between similarly separated points at a given altitude, the horizontal homogeneity due to the cyclic boundary conditions was exploited, and planar averaging was done to achieve less bias in the coherence estimates. At small separations, that is, 20 m, the lateral and vertical coherence is different between the codes. Given the grid size of 10 m, it can be said that coherence at small separations is less reliable and sensitive to the under-resolved small-scale structures. However, at larger separations, the coherence between the codes is quite similar and shows unremarkable differences for the neutral atmospheric precursor, also seen in [22].

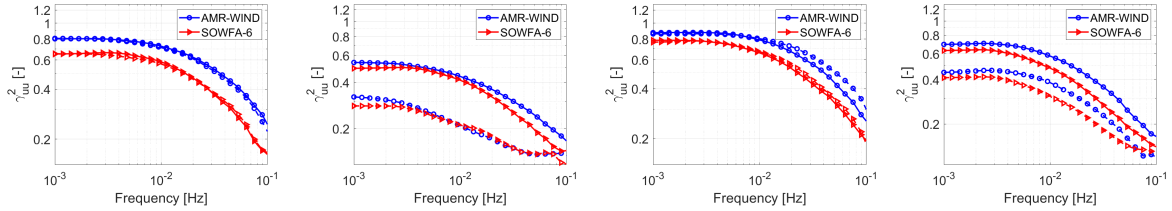

(a) Altitude of 80 m and separation of 20 m (b) Altitude of 80 m and separation of 60 m (c) Altitude of 180 m and separation of 20 m (d) Altitude of 180 m and separation of 60 m

Figure 9: Coherence (solid-vertical, and dashed-lateral separation) estimates for the neutral atmospheric boundary layer precursors generated by AMR-WIND and SOWFA-6, at different altitudes and separations.

The comparison of the spectral characteristics of the precursors with unstable atmospheric conditions generated by the two codes is shown in Figure 10 and Figure 11. It can be observed that AMR-WIND results indicate higher energy in larger wavenumber regions. In comparison, SOWFA-6 results indicate higher energy in the lower wavenumber region of the spectrum (for example, Figure 10b). This contradicts the observation made for the precursors with neutral atmospheric stability. Next, the coherence analysis is shown in Figure 11, further elaborating the spectral characteristics and indicating the coherent structures.

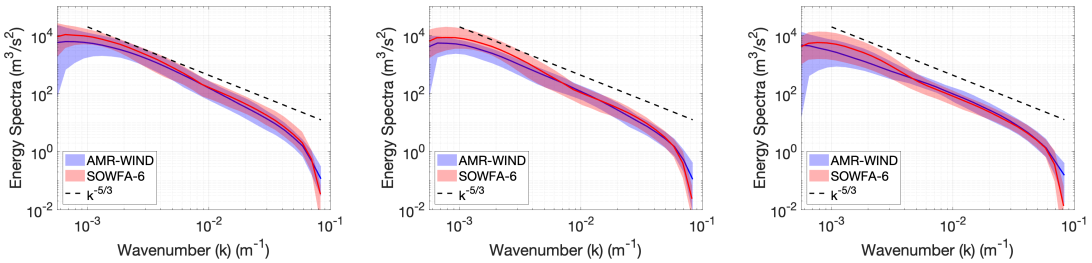

(a) Altitude of 60 m (b) Altitude of 100 m (c) Altitude of 180 m

Figure 10: Energy spectrum for the unstable atmospheric boundary layer precursors generated by AMR-WIND and SOWFA-6, at different altitudes.

In line with the observation that the SOWFA-6 results indicate higher energy in the lower wavenumber region, one can expect that the coherence at lower frequencies, resembling the larger structures, will be higher in SOWFA-6 compared to AMR-WIND. This intuitive result can be observed across all separations, most prominently in Figure 11d. Notable differences are observed between the coherence results of the two codes, particularly in the unstable atmosphere. The coherence at both small and large separations differs between the codes, unlike the coherence comparison in the neutral atmosphere (Figure 9). This finding is significant, and future research involving more codes and measurements can help determine which code provides more accurate results.

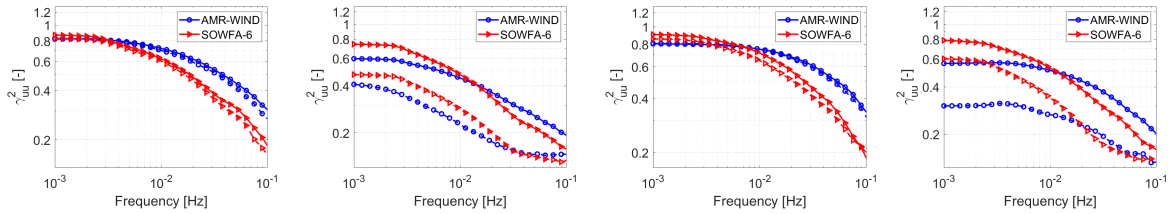

(a) Altitude of 80 m and separation of 20 m (b) Altitude of 80 m and separation of 60 m (c) Altitude of 180 m and separation of 20 m (d) Altitude of 180 m and separation of 60 m

Figure 11: Coherence estimates (solid-vertical and dashed-lateral separation) for the unstable atmospheric boundary layer precursors generated by AMR-WIND and SOWFA-6 at different altitudes and separations.

5 Conclusions

A code-to-code comparison using two widely used LES codes was conducted on NREL SOWFA-6 and AMR-WIND. Uniform inflow wind turbine (IEA 22 MW) wake and load analysis and ABL precursors analysis were conducted. The computational cost of simulations without a turbine in the domain was identical for both solvers. However, the presence of a turbine led to a 35 % faster computational time using AMR-Wind. A longer wind turbine wake was observed in uniform inflow wake conditions in AMR-WIND, partly attributed to the lower diffusion due to the higher order scheme in comparison to SOWFA-6, for the advection terms. For instance, the Reynolds stresses developed after 5 D in SOWFA-6 and after 6 D in AMR-WIND. The difference is expected to be reduced in unsteady and non-uniform inflow conditions, a topic of further research. SOWFA-6 required more actuator points (75) across the blade compared to AMR-WIND (59 - equal to number of defined airfoil sections) for smooth velocity profiles. Regarding the atmospheric boundary layers generated, an excellent agreement in time and frequency domain was observed between the codes, for neutral conditions. However, notable differences were observed in unstable conditions, with differences in coherence at small and large separations at various altitudes. Energy distribution at the largest and smallest wavenumber region of the spectrum differed between the codes, while a near-perfect agreement was seen in the inertial range of the spectrum and the resulting cut-off wavenumber. Future studies incorporating more codes and measurements will aid in deciding which code provides more accurate results.

Acknowledgments
This research was supported by the Korea Institute of Energy Technology Evaluation and Planning (KETEP) grant funded by the Korea Government (MOTIE) (20228520020050). This work has been supported by the SUDOCO project, which receives funding from the European Union's Horizon Europe Programme under grant No. 101122256. The authors thank the Delft High-Performance Computing Centre (https://www.tudelft.nl/dhpc) [23] for the use of computational resources of the DelftBlue supercomputer. The authors thank SURF (www.surf.nl) for the support in using the Dutch National Supercomputer Snellius.

References

[1] Churchfield M, Lee S, Moriarty P, Martinez L, Leonardi S, Vijayakumar G and Brasseur J 2012 A large-eddy simulation of wind-plant aerodynamics *50th AIAA aerospace sciences meeting including the new horizons forum and aerospace exposition* p 537

[2] Martínez-Tossas L A, Churchfield M J, Yilmaz A E, Sarlak H, Johnson P L, Sørensen J N, Meyers J and Meneveau C 2018 *Journal of Renewable and Sustainable Energy* **10** 033301 ISSN 1941-7012 (*Preprint* https://pubs.aip.org/aip/jrse/article-pdf/doi/10.1063/1.5004710/19755870/033301_1_online.pdf) URL https://doi.org/10.1063/1.5004710

[3] SOWFA-6 2020 Nrel simulator for offshore wind farm applications URL https://github.com/NREL/SOWFA-6/pull/22

[4] Exawind 2023 Amr-wind: Adaptive mesh refinement for wind accessed: 2025-01-23 URL https://github.com/Exawind/amr-wind

[5] Churchfield M, Lee S and Moriarty P 2012 URL http://wind.nrel.gov/designcodes/simulators/sowfa/

[6] Sharma A, Brazell M J, Vijayakumar G, Ananthan S, Cheung L, deVelder N, Henry de Frahan M T, Matula N, Mullowney P, Rood J, Sakievich P, Almgren A, Crozier P S and Sprague M 2024 *Wind Energy* **27** 225–257 URL https://onlinelibrary.wiley.com/doi/abs/10.1002/we.2886

[7] Zahle F, Barlas A, Lønbæk K, Bortolotti P, Zalkind D, Wang L, Labuschagne C, Sethuraman L and Barter G 2024 Definition of the IEA Wind 22-Megawatt Offshore Reference Wind Turbine Tech. Rep. DTU Wind Report E-0243, https://doi.org/10.11581/DTU.00000317 Technical University of Denmark, International Energy Agency

[8] Weller H G, Tabor G, Jasak H and Fureby C 1998 *Computers in physics* **12** 620–631

[9] Zhang W, Almgren A, Beckner V, Bell J, Blaschke J, Chan C, Day M, Friesen B, Gott K, Graves D, Katz M, Myers A, Nguyen T, Nonaka A, Rosso M, Williams S and Zingale M 2019 *Journal of Open Source Software* **4** 1370 URL https://doi.org/10.21105/joss.01370

[10] Borges R, Carmona M, Costa B and Don W S 2008 *Journal of Computational Physics* **227** 3191–3211 ISSN 0021-9991

[11] (NREL) N R E L 2023 Openfast: A wind turbine simulation software accessed: 2025-01-23 URL https://github.com/OpenFAST/openfast

[12] Gadde S N and Stevens R J 2021 *Journal of Renewable and Sustainable Energy* **13** 13305 ISSN 19417012 URL /aip/jrse/article/13/1/013305/284849/Effect-of-low-level-jet-height-on-wind-farm

[13] Zahle F, Barlas T, Lønbæk K, Bortolotti P, Zalkind D, Wang L, Labuschagne C, Sethuraman L, Barter G and Marten D 2024 Ieawindtask37/iea-22-280-rwt: v1.0.1 URL https://doi.org/10.5281/zenodo.10944127

[14] Sullivan P P and Patton E G 2011 *Journal of the Atmospheric Sciences* **68** 2395–2415 ISSN 0022-4928 URL https://journals.ametsoc.org/view/journals/atsc/68/10/jas-d-10-05010.1.xml

[15] Dangi N, Sodja J, Ferreira C S and Yu W 2025 *Renewable Energy* **241** 122248 ISSN 0960-1481 URL https://www.sciencedirect.com/science/article/pii/S0960148124023164

[16] Moeng C H 1984 *Journal of Atmospheric Sciences* **41** 2052 – 2062 URL https://journals.ametsoc.org/view/journals/atsc/41/13/1520-0469_1984_041_2052_alesmf_2_0_co_2.xml

[17] Deardorff J W 1980 *Boundary-Layer Meteorology* **18** 495–527 ISSN 1573-1472 URL https://doi.org/10.1007/BF00119502

[18] Nathan J, Masson C and Dufresne L 2018 *Wind Energy Science* **3** 905–917 URL https://wes.copernicus.org/articles/3/905/2018/

[19] Martínez-Tossas L A and Meneveau C 2019 *Journal of Fluid Mechanics* **863** 269–292

[20] Ekaterinaris J A 2005 *Progress in Aerospace Sciences* **41** 192–300 ISSN 0376-0421 URL https://www.sciencedirect.com/science/article/pii/S0376042105000473

[21] Kristensen L and Jensen N O 1979 *Boundary-Layer Meteorology* **17** 353–373 ISSN 15731472 URL https://link.springer.com/article/10.1007/BF00117924

[22] Ning X, Krutova M and Bakhoday-Paskyabi M 2021 *Journal of Physics: Conference Series* **2018** 12027 URL https://dx.doi.org/10.1088/1742-6596/2018/1/012027

[23] (DHPC) D H P C C 2024 URL https://www.tudelft.nl/dhpc/ark:/44463/DelftBluePhase2